Available online at www.sciencedirect.com

ScienceDirect

IFAC PapersOnline CONFERENCE PAPER ARCHIVE

IFAC PapersOnLine 58-20 (2024) 229–234

Experimental Identification of Decoupled Ship Dynamic Models for an Autonomous Catamaran Urban Cargo Vessel ⋆

Yan-Yun Zhang * **Jef Billet** * **Peter Slaets** *

* *Department of Mechanical Engineering, KU Leuven, 3000 Leuven, Belgium (e-mail: yanyun.zhang@kuleuven.be, jef.billet@kuleuven.be, peter.slaets@kuleuven.be)*

Abstract: KU Leuven developed and launched the *Maverick* catamaran in 2023, designed specifically for autonomous cargo transportation in narrow urban waterways. This vessel features a distinct actuation system utilizing two 360-degrees-steerable azimuth thrusters, positioned at the bow and stern. This study proposes and experimentally identifies decoupled ship dynamic models for the *Maverick* that concentrate on surge and yaw. The models aim to predict the vessel's speed and heading, particularly when steered by a bow thruster, sailing stably around service speed along the waterway. To do so, two sets of experiments were designed, each dedicated to collecting data for the individual identification of the decoupled models. These experiments deviate from the conventional use of standard maneuvers such as zigzag or turning, which are intended for maneuverability assessment of sea-going rudder-propeller vessels. Instead, sinusoidal excitation maneuvers were employed to better suit the dynamic system of the *Maverick* with its unique actuation system and operational strategy. Finally, a comparison is made between model predictions and a manually executed waterway-following maneuver recorded for reference. The results underline the suitability of the identified models for accurate trajectory prediction during the stable sailing scenario with small external disturbance and minor course curvature.

Keywords: Autonomous; Identification; Dynamic model; Decoupled; Sinusoidal excitation; Azimuth thruster.

1. INTRODUCTION

Autonomous Surface Vessels (ASVs) are extensively used for different tasks, including environmental monitoring, marine resources exploitation, offshore structures management, surveillance, passenger and cargo transportation, and so on. These rapid proliferation of ASVs applications has heightened the necessity for new technologies to support these varied tasks. In response, numerous research groups around the world are designing experimental ASV platforms with novel actuation systems, moving beyond conventional rudder-propeller configurations to achieve superior maneuverability, enhanced redundancy, and other advancements. Examples sorted by actuation type, include:

- Differential thrust: Defilippo et al. (2019); Roasto et al. (2021).
- Azimuth thrust: Hou et al. (2022); Paasche et al. (2023).
- Water jets: Wu et al. (2009); Machado et al. (2014).

Aligning with this trend, KU Leuven developed the *Maverick*, Zhang et al. (2023), an over-actuated ASV specifically designed for enhanced maneuverability and tailored for cargo transportation in small urban waterways. The *Maverick* is equipped with two 360-degree-steerable azimuth thrusters, one at the bow and one at the stern, rendering it over-actuated.

For over-actuated azimuth-propelled vessels, addressing the thrust allocation problem is crucial. Solutions have been proposed using pseudo-inverse, Sørdalen (1997), dynamic, Liao et al. (2007), and mathematical programming approaches, Billet et al. (2023). Thrust allocation controllers, in turn, are typically employed in maneuvers such as dynamic positioning, Veksler et al. (2016); or automatic docking, Bitar et al. (2020). However, *simple sailing* does not mandate the full use of available actuators. Instead, the choice of an artificially under-actuated thrust configuration, i.e., neglecting certain actuator Degrees of Freedom (DoFs), may benefit the control effort of individual actuators despite omitting an optimization-based allocation method. Therefore, we developed an operating philosophy for the *Maverick* that is applied when the vessel maintains a stable course along the waterway around the service

⋆ The first author Yan-Yun Zhang is a researcher funded by the European Union's Horizon 2020 research and innovation programme under the Marie Skłodowska-Curie grant agreement No 955.768 (MSCA-ETN AUTOBarge). This publication reflects only the authors' view, exempting the European Union from any liability. Project website: `https://etn-autobarge.eu/`. The research vessel was funded by AVATAR project, co-financed by the European Union from the EU Interreg North Sea Region 2014–2020 (European Regional Development Fund). Project website: `https://northsearegion.eu/avatar/`.

10.1016/j.ifacol.2024.10.059

speed. In this scenario, the advancing speed is controlled by the stern thruster, and the steering is controlled by the bow thruster. This necessitates the modeling of its now under-actuated behavior as a bow thruster-steered vessel, which we will demonstrate in this paper. This work will present decoupled dynamic model structures for surge and yaw motions, along with their experimental identification.

The rest of this paper is organized as follows: Section 2 introduces the testing platform, which includes the vessel and the corresponding sensor setup. Subsequently, Section 3 formulates the research problem, encompassing the application scenario, operational strategy, modeling assumptions, and structures of the decoupled ship dynamic models. Next, Section 4 explains the applied methodology, including the experiment design and identification method. Section 5 presents the modeling results and a trajectory comparison between model predictions and a manually executed maneuver. Finally, Section 6 concludes this paper.

2. PLATFORM

Table 1 presents the main particulars of the *Maverick*. Fig. 1 provides illustration of its geometric shape. Fig. 2 demonstrates the actuation system configuration of the *Maverick*: two identical thrusters are placed in separate cylinder cabins under the bridge deck, one at the bow and one at the stern, aligned along the centerline. Each thruster comprises an electric 360-degrees-rotatable saildrive (SDK-ED 2.5 AC) and a propeller. Control for each thruster is achieved by a pair of identical programmable AC motor controllers (Curtis 1232E-2321) managing the azimuth angle denoted as α, and propeller revolution denoted as n.

Table 1. Main particulars of the *Maverick*.

Particular	Symbol/Acronym	Values	Units
Length overall	LOA	6.10	m
Breadth overall	B	2.02	m
Breadth demi-hull	b	0.66	m
Separation distance	S	0.64	m
Moulded depth	D	0.73	m

The *Maverick* is designed to accommodate different sensor setups and data acquisition systems. It treats sensors as external devices rather than fixed onboard components. In this study, a mobile sensor box was deployed to acquire data. Specifically, it comprises the AsteRx-i3 D Pro+ Global Navigation Satellite System (GNSS)/Inertial Navigation System (INS) receiver with dual antennas, which was utilized to acquire the measurements for this research.

3. PROBLEM FORMULATION

This section is dedicated to formulating the research problem addressed by this study: analyzing the application scenario 3.1, devising the operational strategy 3.2, outlining the modeling assumptions 3.3, and constructing the decoupled ship dynamic models 3.4.

3.1 Application Scenario

The transportation journey of inland cargo vessels involves various activities and considerations, which we can summarize into discrete mission phases: (i) Deberthing and

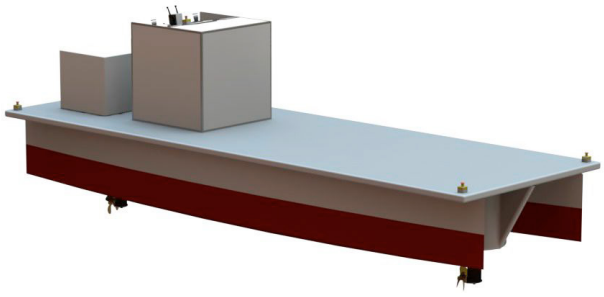

Fig. 1. 3D model representation of the *Maverick*, reproduced from Zhang et al. (2023).

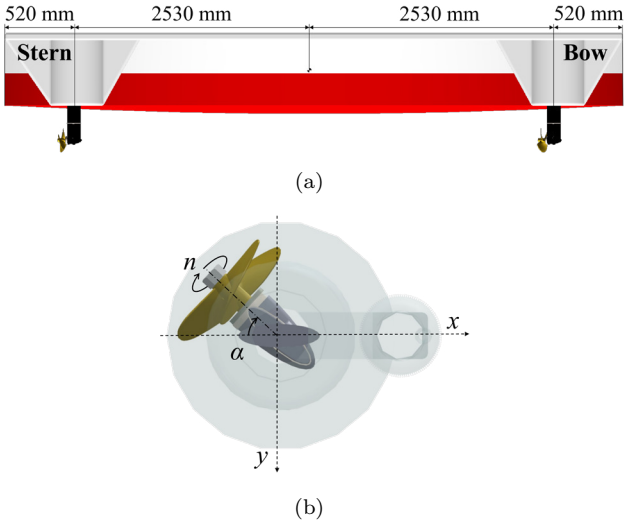

Fig. 2. Actuation system configuration: (a) positions of the thrusters; (b) top view of the thruster.

departure from the port; (ii) Navigation through inland waterways; (iii) Arrival at the port and berthing. The first and third phases mainly involve port maneuvers featuring low speed and sharp turns, while the second phase mainly consists of stable sailing around service speed along the waterway. Note that, navigation through inland waterways also entails intricate maneuvering behaviors, including passing locks and bridges, encountering other vessels, following large waterway bends, and more. This study solely focuses on the stable sailing scenario of the second mission phase.

3.2 Operational Strategy

Given the actuation configuration detailed in Section 2, the *Maverick* exhibits over-actuation in its horizontal motions. While this feature enables distinctive maneuvers such as pivoting around itself or executing parallel docking, it becomes less practical during stable sailing scenario where the vessel follows a continuous path without requiring significant maneuvers. Over-actuating the *Maverick* introduces complexities, necessitating the development of a thruster allocation algorithm to fully exploit the advantages of this setup. This poses challenges related to computational complexity, numerical sensitivity, verification and validation as indicated in Johansen and Fossen (2013). Moreover, this approach may lead to increased control effort, requiring more energy and exertion from the ac-

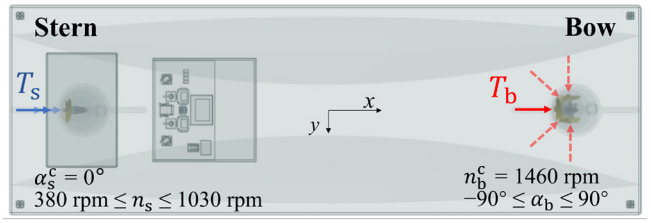

Fig. 3. Operational strategy: advancing with the stern thruster, steering with the bow thruster.

tuators to achieve the desired maneuvers. This heightened demand could accelerate wear and tear on the actuators, potentially leading to increased maintenance costs and reduced longevity of the vessel's propulsion system. As a result, while over-actuation offers unique maneuvering capabilities, its practicality in scenarios like stable sailing may be limited by these drawbacks. Instead, an operational strategy that restricts control freedom and constrains the *Maverick* to an under-actuated state is devised, as also visually demonstrated in Fig. 3.

The azimuth angle of the stern thruster is fixed at 0°—α_s^c, while its propeller revolutions per minute (rpm), n_s, ranges from 380 to 1030; The propeller rpm of the bow thruster is maintained at 1460—n_b^c, while its azimuth angle, α_b, ranges from –90° to 90°. The stern thruster generates thrust T_s with a fixed direction and changing magnitude, regulating the speed of the *Maverick*. The bow thruster produces thrust T_b with a constant magnitude and changing direction, regulating the heading of the *Maverick*.

3.3 Modeling Assumptions

According to Fossen's robot-like vectorial model for marine craft, Fossen (2011), the maneuvering equations of motion in six DoFs can be represented as:

$$\underbrace{\boldsymbol{M}_{\mathrm{RB}}\dot{\boldsymbol{\nu}} + \boldsymbol{C}_{\mathrm{RB}}(\boldsymbol{\nu})\boldsymbol{\nu}}_{\text{rigid-body forces}} + \underbrace{\boldsymbol{M}_{\mathrm{A}}\dot{\boldsymbol{\nu}} + \boldsymbol{C}_{\mathrm{A}}(\boldsymbol{\nu})\boldsymbol{\nu} + \boldsymbol{D}(\boldsymbol{\nu})\boldsymbol{\nu}}_{\text{hydrodynamic forces}} + \underbrace{g(\boldsymbol{\eta}) + g_0}_{\text{hydrostatic forces}} = \boldsymbol{\tau} + \boldsymbol{\tau}_{\text{external}}\,. \tag{1}$$

Here, $\boldsymbol{\nu} = [u, v, w, p, q, r]^T$ denotes the generalized velocity vector in 6 DoFs, where the first three components (u, v, w) are the linear velocities in surge, sway and heave and (p, q, r) are the angular velocities in roll, pitch and yaw. Meanwhile, $\boldsymbol{\eta} = [x, y, z, \phi, \theta, \psi]^T$ denotes the generalized position and orientation vector accordingly. The matrices $\boldsymbol{M}_{\mathrm{RB}}$, $\boldsymbol{C}_{\mathrm{RB}}$ represent the rigid-body mass matrix and coriolis-centripetal matrix, respectively. The matrix $\boldsymbol{M}_{\mathrm{A}}$ accounts for the added mass, while the matrix $\boldsymbol{C}_{\mathrm{A}}$ reflects the coriolis-centripetal effects caused by $\boldsymbol{M}_{\mathrm{A}}$. The damping matrix is denoted by $\boldsymbol{D}(\boldsymbol{\nu})$. The vector $g(\boldsymbol{\eta})$ includes gravitational and buoyancy forces and moments, while the vector g_0 encompasses the static restoring forces and moments due to ballast systems and water tanks. Finally, $\boldsymbol{\tau}$ represents the vector of control inputs, and $\boldsymbol{\tau}_{\text{external}}$ accumulates all other external environmental forces and moments acting on the vessel.

The following assumptions were made to model the decoupled dynamic motions for the *Maverick* in this study:

(1) The longitudinal position of the vessel's center of gravity is approximable to midship, given the symmetric shape of the hull.
(2) The study considers maneuvering motions in the horizontal plane, neglecting pitch, roll, and heave motions. Sway motion is disregarded, considering the vessel sails mostly straight in a stable sailing scenario. Therefore, the investigated motions include surge and yaw, treated as decoupled from each other.
(3) The dynamic behavior of the thrusters is neglected, assuming that the thrust magnitude is solely related to n.
(4) As the experiments were conducted under calm weather conditions, all environmental forces and moments are excluded.

3.4 Decoupled Ship Dynamic Models

Given the modeling assumptions discussed in Section 3.3, equation (1) can be simplified to:

$$(\boldsymbol{M}_{\mathrm{RB}} + \boldsymbol{M}_{\mathrm{A}})\dot{\boldsymbol{\nu}} + \boldsymbol{D}(\boldsymbol{\nu})\boldsymbol{\nu} = \boldsymbol{\tau}\,, \tag{2}$$

where $\boldsymbol{\nu}$ is reduced to $[u, r]^T$. The expression of each matrix can be further written as:

$$\begin{aligned} \boldsymbol{M}_{\mathrm{RB}} &= \begin{bmatrix} m & 0 \\ 0 & I_z \end{bmatrix}, \; \boldsymbol{D}(\boldsymbol{\nu}) = \begin{bmatrix} -X_{uu}u & 0 \\ 0 & -N_r \end{bmatrix}, \\ \boldsymbol{M}_{\mathrm{A}} &= \begin{bmatrix} m_x & 0 \\ 0 & J_z \end{bmatrix}, \quad \boldsymbol{\tau} = \begin{bmatrix} T_{\mathrm{s}} + T_{\mathrm{b}}\cos(\alpha_{\mathrm{b}}) \\ T_{\mathrm{s}}\sin(\alpha_{\mathrm{b}})x_{\mathrm{b}} \end{bmatrix} \\ &= \begin{bmatrix} T_{nn}^{\mathrm{s}} {n_{\mathrm{s}}}^2 + T_{nn}^{\mathrm{b}} {n_{\mathrm{b}}^{\mathrm{c}}}^2 \cos(\alpha_{\mathrm{b}}) \\ T_{nn}^{\mathrm{b}} {n_{\mathrm{b}}^{\mathrm{c}}}^2 \sin(\alpha_{\mathrm{b}})x_{\mathrm{b}} \end{bmatrix}. \end{aligned} \tag{3}$$

Here, m denotes the mass of the ship, while m_x represents the added mass in surge. The moment of inertia is denoted as I_z, and J_z represents the added moment of inertia. The coefficient for surge damping force is X_{uu}, and N_r denotes the coefficient for yaw damping moment. Coefficients associated with the thrusts generated by the stern and bow thrusters are represented by T_{nn}^{s} and T_{nn}^{b}, respectively. Additionally, x_{b} is the longitudinal coordinate of bow thruster position.

Separating the components, the speed model can be written as:

$$(m + m_x)\dot{u} = X_{uu}u^2 + T_{nn}^{\mathrm{s}} {n_{\mathrm{s}}}^2 + T_{nn}^{\mathrm{b}} {n_{\mathrm{b}}^{\mathrm{c}}}^2 \cos(\alpha_{\mathrm{b}})\,, \tag{4}$$

while the heading model can be written as:

$$(I_z + J_z)\dot{r} = N_r r + T_{nn}^{\mathrm{b}} {n_{\mathrm{b}}^{\mathrm{c}}}^2 \sin(\alpha_{\mathrm{b}})x_{\mathrm{b}}\,. \tag{5}$$

By consolidating the unknown coefficients and known constants, equation (4) and equation (5) can be reorganized as:

$$\dot{u} = k_1 u^2 + k_2 {n_{\mathrm{s}}}^2 + k_3 \cos(\alpha_{\mathrm{b}})\,, \tag{6}$$

$$\dot{r} = k_4 r + k_5 \sin(\alpha_{\mathrm{b}})\,, \tag{7}$$

where,

$$k_1 = X_{uu}/(m + m_x)\,, k_2 = T^{\mathrm{s}}_{nn}/(m + m_x)\,,$$
$$k_3 = T^{\mathrm{b}}_{nn} {n^{\mathrm{c}}_{\mathrm{b}}}^2/(m + m_x)\,, \quad (8)$$
$$k_4 = N_r/(I_z + J_z)\,, k_5 = T^{\mathrm{s}}_{nn} {n^{\mathrm{c}}_{\mathrm{b}}}^2 x_{\mathrm{b}}/(I_z + J_z)\,.$$

Here, k has subscripts ranging from 1 to 5 denoting the unknown coefficients that need to be identified.

4. METHODOLOGY

The methodology is divided into Section 4.1, which explains the design of the experiments committed to collect data for identification, and Section 4.2, which introduces the identification method utilized for the experiment.

4.1 Experiment Design

To achieve high identification modeling accuracy, experiments must be carefully designed to appropriately excite the model. The performance of the identified model heavily depends on whether the excitation signal contains enough information of the system, as suggested in Zhang et al. (2022). Standard maneuvers such as 20°/20° and 10°/10° zigzag maneuvers, and 35° turning circle maneuver have been widely used in literature. However, it is important to note that these maneuvers were originally proposed to evaluate ship maneuverability of conventional rudder-propeller vessels, rather than providing data for identification modeling vessels with atypical actuation layouts.

Given the operational strategy detailed in Section 3.2, there are two controllable system inputs: n_{s} ranging from 380 rpm to 1030 rpm and α_{b} ranging from –90° to 90°. Two sets of experiments were designed with the aim of isolating each control input, studying how the system responds to variations in one control input while keeping the other one fixed:

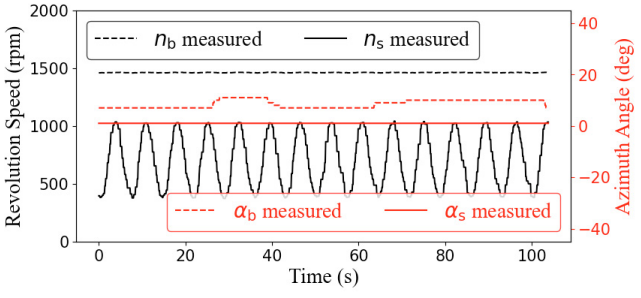

(a)

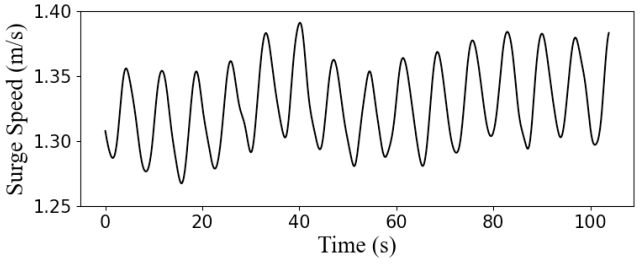

(b)

Fig. 4. ***Experiment I*:** (a) n_{s} changing sinusoidally, α_{b} setting at neutral helm; (b) corresponding response of u.

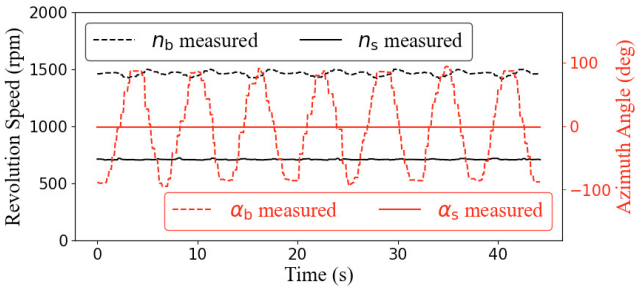

(a)

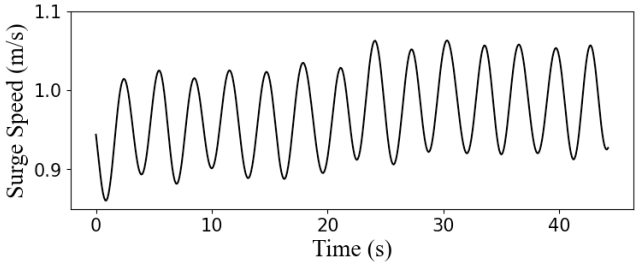

(b)

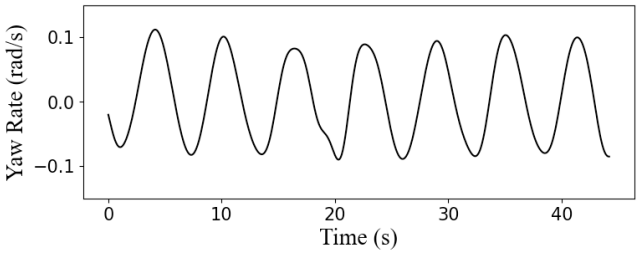

(c)

Fig. 5. ***Experiment II*:** (a) α_{b} changing sinusoidally, n_{s} setting at 710 rpm; (b) corresponding response of u; (c) corresponding response of r.

(1) ***Experiment I***: Applying a sinusoidal input of n_{s}, while keeping α_{b} constant at the neutral helm position, as depicted in Fig. 4(a). It is important to note that (i) α_{b} is not completely constant in order to keep the heading angle to 0°, and (ii) neutral helm is not set at 0°, due to the asymmetric steering behavior, as reported in Zhang et al. (2023). Fig. 4(b) shows the corresponding response of u.

(2) ***Experiment II***: Applying a sinusoidal input of α_{b}, while giving a constant n_{s} command, as shown in Fig. 5(a). Note that the measured n_{b} exhibits fluctuations along with the changing α_{b}, even with a constant command. Fig. 5(b) and Fig. 5(c) show the corresponding response of u and r respectively.

A bias can be observed in the response of r due to the asymmetric steering characteristic of the *Maverick*, as shown in Fig. 5(c). Equation (7) is modified accordingly by adding a bias term k_6:

$$\dot{r} = k_4 r + k_5 \sin(\alpha_{\mathrm{b}}) + k_6\,. \quad (9)$$

The heading model is only excited by α_{b}, whereas the speed model is excited by both of the control inputs. I.e., ***Experiment II*** is sufficient for the heading model

construction while both ***Experiment I*** and ***Experiment II*** are needed for the speed model identification.

4.2 Identification Method

The unknown parameters in the decoupled models were identified using a bounded nonlinear least squares algorithm implemented with the *SciPy* package, Virtanen et al. (2020). The trust-region reflective method is used to solve the bound-constrained minimization problem, as formulated in Branch et al. (1999). The algorithm iteratively solves trust-region sub-problems augmented by a diagonal quadratic term and with the trust-region shape determined by the distance from the bounds and the direction of the gradient. The cost functions $E_{\dot{u}}(\boldsymbol{\theta}_{\dot{\boldsymbol{u}}})$ and $E_{\dot{r}}(\boldsymbol{\theta}_{\dot{\boldsymbol{r}}}, \beta_{\dot{r}})$ can be written as:

$$E_{\dot{u}}(\boldsymbol{\theta}_{\dot{\boldsymbol{u}}}) = \sum_{i=1}^{i=\ell} E_{\dot{u}_i}(\boldsymbol{\theta}_{\dot{\boldsymbol{u}}}) \tag{10}$$
$$= \sum_{i=1}^{i=\ell} \left(\dot{u}_i - \hat{\dot{u}}_i\left(u_i, n_{\mathrm{s}_i}, \alpha_{\mathrm{b}_i}, \boldsymbol{\theta}_{\dot{\boldsymbol{u}}}\right)\right)^2,$$

$$E_{\dot{r}}(\boldsymbol{\theta}_{\dot{\boldsymbol{r}}},\ \beta_{\dot{r}}) = \sum_{i=1}^{i=\ell} E_{\dot{r}_i}(\boldsymbol{\theta}_{\dot{\boldsymbol{r}}},\ \beta_{\dot{r}}) \tag{11}$$
$$= \sum_{i=1}^{i=\ell} \left(\dot{r}_i - \hat{\dot{r}}_i\left(r_i, \alpha_{\mathrm{b}_i}, \boldsymbol{\theta}_{\dot{\boldsymbol{r}}}, \beta_{\dot{r}}\right)\right)^2.$$

Here, $\boldsymbol{\theta}_{\dot{\boldsymbol{u}}} = [k_1, k_2, k_3]^T$ and $\boldsymbol{\theta}_{\dot{\boldsymbol{r}}} = [k_4, k_5]^T$ denote the parameter vector of the speed model and heading model, respectively. The bias term of the heading model is denoted by $\beta_{\dot{r}} = k_6$, and ℓ represents the number of data samples.

5. EXPERIMENTAL IDENTIFICATION RESULTS

This section presents the modeling results of this study. Table 2 summarizes the identified model parameters.

Table 2. Identified model parameters.

Speed model		Heading model	
Parameters	Values	Parameters	Values
k_1	–0.153	k_4	–0.52
k_2	8e−8	k_5	0.085
k_3	0.23	k_6	0.009

With the identified models, predictions on surge speed and yaw rate can be generated by considering a given initial state and a continuous stream of control inputs:

$$\begin{aligned} \dot{\boldsymbol{x}}(t) &= \boldsymbol{f}\left(\boldsymbol{x}(t), \boldsymbol{c}(t)\right), \\ \boldsymbol{x}(t+h) &= h\dot{\boldsymbol{x}}(t) + \boldsymbol{x}(t). \end{aligned} \tag{12}$$

Here, $\boldsymbol{x}(t) = [u(t), r(t)]^T$ is the state vector and $\boldsymbol{c}(t) = [n_{\mathrm{s}}(t), \alpha_{\mathrm{b}}(t)]^T$ is the control vector at the current time step. The function $\boldsymbol{f}(\cdot)$ composes the right-hand side of (6) and (9). The state vector at the next time step, $\boldsymbol{x}(t+h)$, is determined using the Euler Forward method with a time step length of $h = 0.1$ s. Furthermore, predictions on vessel position and heading at each time step can be calculated using:

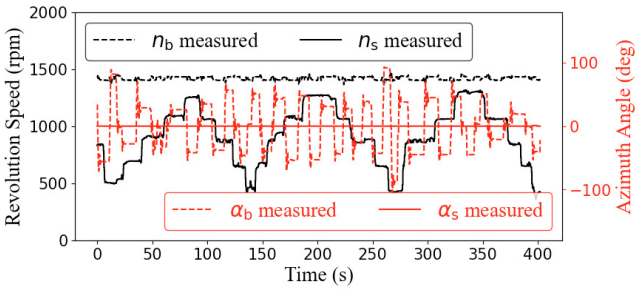

Fig. 6. Control inputs of the manually executed waterway-following maneuver.

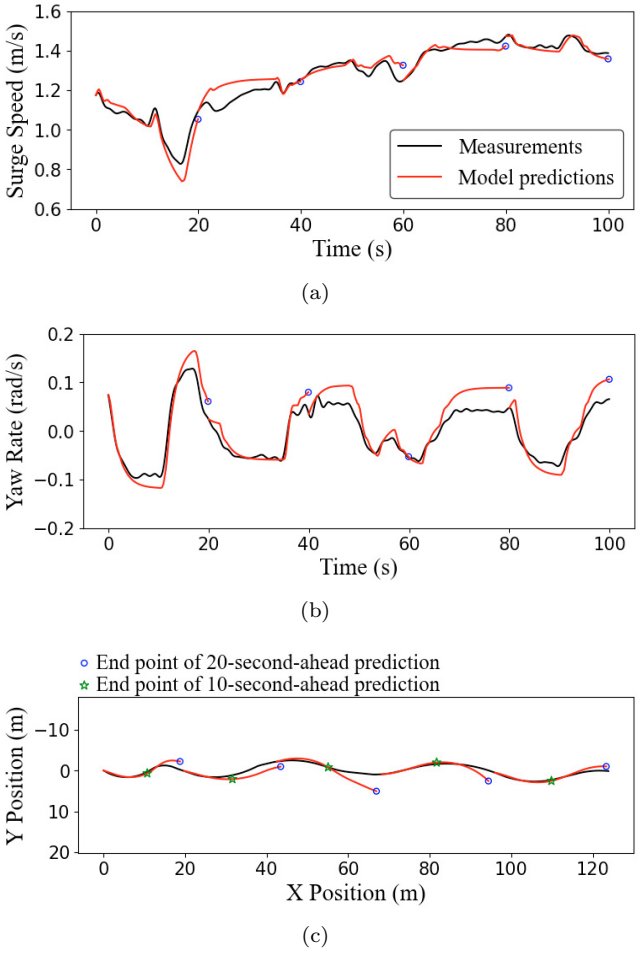

Fig. 7. Model verification results: Comparisons between measurements and 20-second-ahead model predictions over a 100-second timescale for (a) u; (b) r; (c) trajectory of the vessel.

$$\begin{aligned} \dot{x}(t) &= u(t)\cos(\theta(t)), \ \dot{y}(t) = u(t)\sin(\theta(t)), \\ \dot{\theta}(t) &= r(t). \end{aligned} \tag{13}$$

Finally, to verify the model performance under both of the control inputs, a manually executed waterway-following maneuver was recorded as the data source for comparison. During this maneuver, n_{s} and α_{b} changed simultaneously, as shown in Fig. 6, creating an arbitrary combination of excitation for both surge and yaw motions. Fig. 7 presents the comparisons between measurements and 20-second-ahead model predictions over a 100-second timescale. We

can observe that the identified models accurately predict the motion responses induced by the control inputs. Regarding the trajectory prediction shown in Fig. 7(c), the 10-second-ahead prediction demonstrates high accuracy. However, beyond the 10-second mark, the accumulated error becomes more noticeable, leading to slight deviations from the measurements. The results underscore that, within the previously defined stable sailing application scenario, the minor sway motion can be reasonably neglected without significantly impacting the accuracy of trajectory prediction.

6. CONCLUSIONS

This paper models the surge and yaw motions of the *Maverick* within the stable sailing scenario, adhering to the operational philosophy of using the stern thruster for advancement and the bow thruster for steering. Accordingly, modeling assumptions and decoupled model structures are specified. Furthermore, to identify the unknown parameters, two sets of sinusoidal excitation maneuvers, each isolating a control input, were conducted to collect data. The identification process is performed using a bounded nonlinear least squares algorithm. The identified models are validated on the sinusoidal excitation maneuvers first and then verified on a manually executed waterway-following maneuver. The modeling results demonstrate that the proposed models are capable of predicting the vessel trajectory accurately. The reasonable modeling simplifications we made, together with the informative experiment design for data collection, contribute to a pragmatic solution for *simple sailing* of the *Maverick*.

ACKNOWLEDGEMENTS

The authors would like to thank Thibaut Schamp, Jiangtao Shuai, and Amirreza Haqshenas Mojaveri for their help with data collection; Senne Van Baelen and Jan Swevers for comments that have contributed to the improvement of this work.

REFERENCES

Billet, J., Pilozzi, P., Louw, R., Schamp, T., and Slaets, P. (2023). Model predictive and decoupled thrust allocation for overactuated inland surface vessels. In *Proceedings of 21st European Control Conference (ECC)*, 1–6. IEEE. doi:10.23919/ECC57647.2023.10178200.

Bitar, G., Martinsen, A.B., Lekkas, A.M., and Breivik, M. (2020). Trajectory planning and control for automatic docking of ASVs with full-scale experiments. *IFAC-PapersOnLine*, 53(2), 14488–14494. doi:10.1016/j.ifacol.2020.12.1451. 21st IFAC World Congress (WC).

Branch, M.A., Coleman, T.F., and Li, Y. (1999). A subspace, interior, and conjugate gradient method for large-scale bound-constrained minimization problems. *SIAM Journal on Scientific Computing*, 21(1), 1–23.

Defilippo, M., Robinette, P., Sacarny, M., and Benjamin, M.R. (2019). The Remote Explorer IV: an autonomous vessel for oceanographic research. In *Proceedings of OCEANS 2019—Marseille*. IEEE. doi:10.1109/oceanse.2019.8867173.

Fossen, T.I. (2011). *Handbook of marine craft hydrodynamics and motion control*. John Wiley & Sons, Ltd: Chichester, UK.

Hou, L., Chen, S., and Png, Q.S. (2022). Design of a deployable cargo vessel based on autonomous surface vehicle to aid offshore maritime shipping. In *Proceedings of 8th International Conference on Robotics and Artificial Intelligence (ICRAI)*. ACM. doi:10.1145/3573910.3573918.

Johansen, T.A. and Fossen, T.I. (2013). Control allocation—A survey. *Automatica*, 49(5), 1087–1103. doi:10.1016/j.automatica.2013.01.035.

Liao, F., Lum, K.Y., Wang, J.L., and Benosman, M. (2007). Constrained nonlinear finite-time control allocation. In *Proceedings of 26th American Control Conference (ACC)*, 3801–3806. IEEE. doi:10.1109/ACC.2007.4282512.

Machado, D., Martins, A., Almeida, J.M., Ferreira, H., Amaral, G., Ferreira, B., Matos, A., and Silva, E. (2014). Water jet based autonomous surface vehicle for coastal waters operations. In *Proceedings of OCEANS 2014—St. John's*, 1–8. IEEE. doi:10.1109/OCEANS.2014.7003169.

Paasche, M.T., Helgesen, Ø.K., and Brekke, E.F. (2023). Real-time 360 degrees view for the operator of milliAmpere 2. *Journal of Physics: Conference Series*, 2618(1), 012009. doi:10.1088/1742-6596/2618/1/012009. 5th International Conference on Maritime Autonomous Surface Ships (ICMASS).

Roasto, I., Molder, H., Jalakas, T., Moller, T., Tabri, K., and Enok, M. (2021). Design and testing of an universal autonomous surface vehicle. In *Proceedings of 19th International Power Electronics and Motion Control Conference (PEMC)*. IEEE. doi:10.1109/pemc48073.2021.9432567.

Sørdalen, O.J. (1997). Optimal thrust allocation for marine vessels. *Control Engineering Practice*, 5(9), 1223–1231. doi:10.1016/S0967-0661(97)84361-4.

Veksler, A., Johansen, T.A., Borrelli, F., and Realfsen, B. (2016). Dynamic positioning with model predictive control. *IEEE Transactions on Control Systems Technology*, 24(4), 1340–1353.

Virtanen, P., Gommers, R., Oliphant, T.E., Haberland, M., Reddy, T., Cournapeau, D., Burovski, E., Peterson, P., Weckesser, W., Bright, J., et al. (2020). SciPy 1.0: fundamental algorithms for scientific computing in Python. *Nature Methods*, 17(3), 261–272.

Wu, G., Sun, H., Zou, J., and Wan, L. (2009). The basic motion control strategy for the water-jet-propelled USV. In *Proceedings of 6th International Conference on Mechatronics and Automation (ICMA)*, 611–616. IEEE.

Zhang, Y.Y., Shuai, J., Billet, J., and Slaets, P. (2023). Design and build of an autonomous catamaran urban cargo vessel. *Journal of Physics: Conference Series*, 2618(1), 012002. doi:10.1088/1742-6596/2618/1/012002. 5th International Conference on Maritime Autonomous Surface Ships (ICMASS).

Zhang, Y.Y., Wang, Z.H., and Zou, Z.J. (2022). Black-box modeling of ship maneuvering motion based on multi-output nu-support vector regression with random excitation signal. *Ocean Engineering*, 257, 111279. doi:10.1016/j.oceaneng.2022.111279.